Numerical study on complex conductivity characteristics of hydrate-bearing porous media and correlations with saturation

Lanchang Xing[1,*], Shuying Qi[1], Yuan Xu[1], Bin Wang[1], Liyun Lao[2],

Wei Wei[3], Weifeng Han[3], Zhoutuo Wei[4], Xinmin Ge[4], Aliyu M. Aliyu[5]

[1] College of Control Science and Engineering, China University of Petroleum (East China), No. 66, West Changjiang Road, Huangdao District, Qingdao 266580, China

[2] School of Water, Energy and Environment, Cranfield University, Cranfield MK43 0AL, UK

[3] Department of Alternative Energy, PetroChina Research Institute of Petroleum Exploration & Development, Langfang 065007, Hebei, China

[4] School of Geosciences, China University of Petroleum (East China), No. 66, West Changjiang Road, Huangdao District, Qingdao 266580, Shandong, China

[5] School of Computing and Engineering, University of Huddersfield, HD1 3DH, United Kingdom.

* Correspondence: xinglc@upc.edu.cn OR l.xing@yahoo.com

Abstract

The complex conductivity method is frequently used in hydro-/petro-/environmental geophysics, and considered to be a promising tool for characterizing and quantify the properties of subsurface rocks, sediments and soils. We report a study on the complex conductivity characteristics of porous media containing gas hydrates through numerical modelling and analysis of the effects of the hydrate saturation. The effect of pore-water salinity and micro-distribution mode were studied and hydrate-saturation evaluation correlations were developed based on complex conductivity parameters. A pore-scale numerical approach for developing the finite-element based models for hydrate-bearing porous media is proposed and a two-dimensional (2D) model is built to compute the complex conductivity responses of porous media under various conditions. We demonstrate that the simple 2D model can capture the dominant characteristics of the complex conductivity of

hydrate-bearing porous media within the frequency range related to the induced polarization. The in-phase conductivity, quadrature conductivity and effective dielectric constant can be correlated with the saturation based on a power law in a log-log space, by which the hydrate-saturation evaluation models can be derived. A constant saturation exponent of the power-law correlation between the hydrate saturation and quadrature conductivity was obtained when the pore-water conductivity exceeds 1.0 S/m. This is highly desirable in the hydrate-saturation models due to the variations of the pore-water conductivity in the processes of hydrate formation and dissociation. Within the framework of the complex conductivity analysis, the micro-distribution modes of hydrates in porous media can be categorized into two types. These are the fluid-suspending mode and grain-attaching mode. The in-phase conductivity exhibits significant variations under the same saturation and salinity but different micro-distribution modes, which can be attributed to the change in the tortuosity of the electrical conduction paths in the void space of porous media.

Keywords: gas hydrate, complex conductivity, hydrate-bearing porous medium, numerical modelling, hydrate saturation, salinity, micro-distribution mode

1 Introduction

Gas hydrate or clathrate hydrate is a crystalline material resembling ice. In the clathrate hydrate, small molecules of a variety of types are trapped inside cages in rigid, hydrogen-bonded water lattices (Hawkins and Davidson, 1966; Sloan, 2003). In nature, natural gas hydrates are widely available in marine sediments and land permafrost areas, and are considered to be a promising low-carbon-emission energy resource (Makogon, 2010; Boswell and Collet, 2011). It is of vital importance to evaluate hydrate-bearing formations in both the exploration and exploitation stages to achieve efficient and economic development of hydrate reservoirs. Currently, most technologies used for hydrate-reservoir evaluation have been introduced from the engineering applications in the conventional oil and gas industry. It is not surprising that various challenges have risen in terms of the usability, reliability and accuracy of those technologies. This is because hydrate reservoirs have unique characteristics. Gas hydrates exist in a solid state and exhibits several micro-scale distribution modes within the void spaces of the formation. These make understanding and predicting the reservoir physical properties (e.g., the acoustic speed, electrical resistivity, etc.) difficult. Furthermore, gas hydrates can decompose and re-compose if the pressure-temperature conditions deviate from the stability zone. The variable salinity of the pore fluid induced by the decomposition and secondary formation of hydrates poses difficulties to resistivity/conductivity-based techniques for evaluating hydrate-bearing formations (e.g., interpretation of the hydrate saturation, porosity, permeability, etc.).

Solid-state gas hydrates exhibit various microscale-distribution characteristics in porous media. The characteristics are affected by the initial concentration and pore-scale distributions of gas and water (Waite et al., 2004; Lei et al., 2019; Pan et al., 2021; Kou et al., 2021), physical and chemical properties of solid grains and their surfaces (Yun et al., 2005; Ta et al., 2015), and environmental conditions such as the temperature and pressure. Both experimental and numerical approaches have been used to observe the microscopic morphologies of hydrates. These include the direct imaging with X-ray CT or MRI (Kneafsey et al., 2007, 2011; Kerkar et al., 2009; Ta et al., 2015; Sell et al., 2016; Lei et al. 2019; Lv et al., 2020; Ersland et al., 2010; Song et al., 2015), numerical simulations with CFD (Computational Fluid Dynamics), LBM (Lattice Boltzmann Method) or phase field model (Yu et al., 2017; Fukumoto et al., 2018; Chen et al., 2018; Wang et

al., 2019). To obtain physics-based effective medium models for the elastic properties of hydrate-bearing sediments, Dvorkin et al. (2000) modified the model for brine-saturated sediment by placing gas hydrates (present in the pore fluid) in the sediment frame and regarding it as a grain-contact cement. Yun et al. (2005) classified the micro-distribution modes reported by Dvorkin et al. (2000) into three. These are: pore-filling, frame-building and cementation modes. They analyzed the compressional and shear wave velocities of hydrate-bearing fine-grained sands at low confinement. In the study of Fukumoto et al. (2018), the micro-distribution modes reported by Dvorkin et al. (2000) were classified into: floating, load bearing, coating, and bridging types. The hydrates formation process was numerically simulated within the microscopic computational domains based on the classical nucleation theory and the phase-field model. Besides the above three or four micro-distribution modes, Dai et al. (2012) focused on another distribution mode, namely the patchy hydrate-saturation mode which is characterized by patches of hydrate-saturated sands embedded in the water-filled sands. It was shown by the analytical and numerical solutions that tight bounds of the physical properties (such as elastic, electrical, hydraulic and thermal) can be obtained from the patchy mode relative to those assuming homogeneous multicomponent mixtures of the mineral-hydrate-gas or mineral-hydrate-gas-water (Mahabadi et al., 2016, 2019). To investigate the effects of porous materials and pore structures on the occurrence and microstructure of gas hydrates, Zhao et al. (2015) visualized hydrate-bearing sediments using micro-focus X-ray CT. They observed that a water layer coated the grains and the gas hydrates randomly formed in a floating mode (Yang et al., 2015; Spangenberg et al., 2005). To quantitatively investigate the evolution of the pore-scale hydrate morphology in the dissociation process, Wang et al. (2020) identified three micro-distribution modes based on X-ray CT imaging (Li et al., 2019). These states are: interpore hydrate framework, pore-filling, and grain-coating. They claimed that the interpore hydrate framework had a higher value of the shape factor, indicating a more complicated hydrate microstructure. Dong et al. (2018, 2019) constructed a model of hydrate-bearing rocks by digitally combining the CT scanning images of actual rocks and the diffusion limited aggregation model. They investigated the effects of three idealized hydrate micro-distribution modes (namely the adhesive mode, cemented mode and scattered mode) on the resistivity characteristics based on the finite element method. The physical properties of hydrate-bearing porous media, such as the electrical, elastic, thermal and hydraulic properties are

influenced by not only the hydrate saturation but also the micro-distribution modes (Dai et al., 2012). Therefore, the pore-scale distribution characteristics of hydrates have to be taken into account when relating the physical parameters to the hydrate saturation. The reason is because different correlations can be derived for different micro-distribution modes even at the same saturation.

The induced polarization (IP) method for geophysical exploration is based on the low-frequency (typically from few millihertz to few tens of kilohertz, especially lower than 10 kHz in the field.) electrical polarization processes occurring in porous media. Applications of the IP method have been extended to environmental, hydro-/hydrocarbon-/bio-geophysical areas. It has been shown that some physical, chemical and biological characteristics (such as porosity, pore/grain size, permeability, specific surface area, wettability, tortuosity, phase distribution, saturation etc.) of subsurface structures (e.g., various porous media such as soils, rocks, and so on) can be related to the IP responses. The measurement of the IP responses can be implemented either in the time domain or in the frequency domain (called spectral induced polarization, SIP.). The SIP response gives the modulus of the conductivity and the phase shift between the current and voltage, then it can be represented by an equivalent complex conductivity or its reciprocal (i.e., complex resistivity). The electrical polarization processes responsible for the measured complex conductivity spectra of porous media can be classified into two categories. These are the electrochemical polarization and interfacial polarization (Leroy et al., 2008). One process corresponding to the electrochemical contribution is related to the polarization of the electrical double layer (EDL) coating the surface of solid particles. It is assumed that a fixed charge density counterbalanced by charge densities of the Stern and diffuse layers, is located at the surface of particles in contact with the pore water. The other process is the Maxwell-Wagner (MW) polarization caused by the formation of free-charge (induced by the electrical field) distributions near the interface between different components, i.e., the solid particles and the pore water. The MW polarization is an interfacial polarization due to the discontinuity of displacement currents in a multicomponent system (e.g., saturated or unsaturated porous media) with dielectric permittivity and/or electrical conductivity discontinuities at the interfaces between different components. The complex resistivity logging approach has been proposed based on the application of the IP method to boreholes (Freedman, 1986; Worthington and Collar, 1984; Osterman et al.,

2016). It has been used to evaluate the oil saturation and/or flooding degree of water-flooded reservoirs based on the differences of the complex resistivity/conductivity characteristics. Considering the similarity of the electrical properties between oil and hydrate and varying pore water salinities in the hydrate-bearing formation, we propose to evaluate the hydrate saturation based on the complex conductivity characteristics. It is the first step in obtaining and understanding the complex conductivity responses of hydrate-bearing porous media, and quantifying the relationship between the complex conductivity and hydrate saturation.

Obtaining reliable and repeatable measurements of the complex conductivity characteristics of hydrate-bearing porous media through laboratory experiments is challenging (Ishai et al., 2013; Kemna et al., 2012). Firstly, it is difficult to control the macro and micro-scale (i.e., the core/pore-scale) distribution of the inclusions (e.g., water, oil or hydrate) in the porous media. It is also difficult to reproduce the distribution of the mineral-fluid interfaces and pore-throat network. Small differences in sample preparation can result in significant changes in the frequency-dispersion spectra of the complex conductivity. Secondly, the measurement strategy involves several sensitive factors, such as current density and electrode materials. The current density is related to the non-linear effects, signal-to-noise ratio, and polarization of the current electrodes. It also depends on electrode material (e.g., metal and metal-metal salts), on shape (e.g., point and ring), on spatial allocation (related to errors resulting from the polarization of the current electrodes), on cable-coupling and capacitive coupling. The measurement strategy also depends on calibration (e.g., against the resistor-capacitor circuits and other reference materials), and data processing method (e.g., removal of the electromagnetic effects and estimation of errors). Bearing the aforementioned challenges in mind, we turn to the pore-scale numerical modelling approach for performing repeatable numerical experiments under controlled conditions. additionally, a large amount of data were generated of the complex conductivity responses over a wide range of test parameters (test frequencies, saturations, salinities and micro-distribution modes).

In this work, we propose a pore-scale numerical approach for developing the finite-element based models to compute the complex-conductivity responses of hydrate-bearing porous media. The effects of hydrate

saturation, salinity of the pore fluid and hydrate micro-distribution mode on the frequency-dispersive complex conductivity are analyzed based on solutions from the numerical models. Correlations are derived between the hydrate saturation and hydrate-bearing porous media complex conductivity. The correlations account for the effects of pore-fluid salinity and pore-scale micro-distribution modes and serve as potential models for evaluating the hydrate saturation in sediments.

2 Complex conductivity of porous medium and micro-distribution of hydrate

2.1 Complex conductivity of water-saturated porous media

Directional movements of free charges and displacements of bound charges are induced in a medium submitted to an electrical field. The total current density resulting from an alternating electrical field is the sum of the conduction and displacement current densities (Tarasov and Titov, 2013). It is given by the right-hand term of Eq (1) obtained from the Ampere's law:

$$\nabla \times \mathbf{H}=\mathbf{J}_{\mathbf{c}}+\frac{\partial \mathbf{D}}{\partial t} \tag{1}$$

where $\mathbf{H}$ is the magnetic field intensity (in A/m), $\mathbf{J_c}$ is the conduction-current density (in A/m^2) according to the Ohm's law, t is time (in s) and $\mathbf{D} = \varepsilon_0\varepsilon\mathbf{E}$ is the dielectric displacement (in C/m^2) according to Maxwell's first equation. The symbols ε_0 and ε are the conductivity (in S/m), vacuum permittivity ($\varepsilon_0 = 8.854\times10^{-12}$ F/m) and relative permittivity (or called dielectric constant, dimensionless), respectively. Usually, the electrical field intensity $\mathbf{E}$ takes the form of a harmonic $\mathbf{E} = \mathbf{E_0}\exp(\mathrm{i}\omega t)$ with the angular frequency of ω ($\omega = 2\pi f$, f in Hz and ω in rad/s).

Considering that the electrical conductivity as a complex number (i.e., complex conductivity σ^*), we can write the total current density ($\mathbf{J_t}$) as Eq (2) according to the Ohm's law.

$$\mathbf{J}_{\mathbf{t}}=\sigma\mathbf{E}+\mathrm{i}\omega\varepsilon_0\varepsilon\mathbf{E}=\sigma^*\mathbf{E} \tag{2}$$

where $\sigma=\sigma'+\mathrm{i}\sigma''$ and $\varepsilon=\varepsilon'+\mathrm{i}\varepsilon''$ are complex scalars dependent on the frequency of $\mathbf{E}$, and the complex

conductivity $\sigma^*=\sigma+\mathrm{i}\omega\varepsilon_0\varepsilon$ fully describes the electrical behavior of a medium incorporating both the electrical conduction and polarization mechanisms. The complex conductivity can also be expressed with the effective conductivity and relative permittivity as below:

$$\sigma^*=\sigma_{\text{eff}}+\mathrm{i}\omega\varepsilon_0\varepsilon_{\text{eff}} \tag{3}$$

where $\sigma_{\text{eff}}=\sigma'-\omega\varepsilon_0\varepsilon''$ and $\varepsilon_{\text{eff}}=\varepsilon'+\sigma''/\omega\varepsilon_0$ are real frequency-dependent scalars and called the effective conductivity and effective relative permittivity (or effective dielectric constant), respectively. Each of σ_{eff} and ε_{eff} incorporates contributions from both the conduction and polarization mechanisms, which are exactly the parameters directly obtained from experimental measurements.

The Stern layer is the inner part of the EDL. According to the Stern layer polarization model developed by Revil and co-workers (Leroy et al, 2008; Revil et al, 2012; Revil, 2013; Revil et al., 2013; Revil et al., 2017ab), the complex conductivity of a granular material saturated with a fluid can be written as:

$$\sigma^*=\frac{1}{F}\left[\sigma_f^*+\left(F-1\right)\sigma_s^*\right] \tag{4}$$

where $\sigma_f^*=\sigma_f+i\omega\varepsilon_0\varepsilon_f$ is the complex conductivity of the pore fluid (in S/m, and the subscript *f* stands for the fluid), ε_f is the dielectric constant of the fluid (e.g., water solution), σ_s^* denotes the complex-valued surface conductivity (i.e., the equivalent complex conductivity of the solid particles coated by the EDL, in S/m, and the subscript *s* stands for the solid phase as well as the surface of solid particles), F is the intrinsic formation factor (it is dimensionless and does not account for surface conduction) related to the connected porosity ϕ by the Archie's law $F=\phi^{-m}$, and m is the cementation exponent (Archie, 1942). Consider a porous medium made of spherical silica grains with the same diameter d_0 (i.e., Dirac distribution of the grain size, in m) and which is saturated by an electrolyte solution (i.e., the pore fluid such as a binary monovalent

electrolyte NaCl). The complex surface conductivity can be calculated through a convolution computation of the complex conductivity response for a Dirac distribution of the grain size with the specific grain-size-distribution function. This can be done for the case of insulating grains coated by a conductive and fixed layer and a porous medium characterized by a certain grain size distribution, The complex-valued conductivity σ_s^* (i.e., the equivalent complex conductivity of the solid grains) can be decomposed into two components, i.e., an in-phase component $\sigma_s^{'}(\omega)$ and a quadrature component $\sigma_s^{''}(\omega)$ as shown in Eqs. (5)-(7).

$$\sigma_s^*(\omega)=\sigma_s^{'}(\omega)+\mathrm{i}\sigma_s^{''}(\omega) \tag{5}$$

$$\sigma_s^{'}(\omega)=\sigma_s^{\infty}+\frac{\sigma_s^0-\sigma_s^{\infty}}{1+\omega^2\tau_0^2} \tag{6}$$

$$\sigma_s^{''}(\omega)=\frac{(\sigma_s^{\infty}-\sigma_s^0)\omega\tau_0}{1+\omega^2\tau_0^2} \tag{7}$$

where $\tau_0=\frac{d_0^2}{8D_{(+)}^S}$ is the relaxation time calculated from the diffusing coefficient (in m/s) of counterions in the Stern layer $D_{(+)}^S$ (which can be related to the mobility of counterions in the Stern layer by the Nernst-Einstein relationship (Revil, 2013), and the superscript *S* stands for the Stern layer.), σ_s^0 and σ_s^{∞} are the low and high-frequency asymptotic limits of the surface conductivity calculated by Eqs. (8) and (9), respectively.

$$\sigma_s^0=\frac{4}{d_0}\Sigma_S^0 \tag{8}$$

$$\sigma_s^{\infty} = \frac{4}{d_0}\left(\sum_S^0 + \sum_S^{\infty}\right) \tag{9}$$

where $\sum_S^0$ is the DC (direct current) specific surface conductivity (in Siemens) that results from the electromigration in the diffuse layer and from the protons of the water adsorbed onto the grain surface, and $\sum_S^{\infty}$ is the specific surface conductivity from the contribution of the Stern layer at high frequencies. The two specific surface conductivities can be computed by Eqs. (10) and (11), respectively.

$$\Sigma_S^0 = \beta_{(+)}^S e\Gamma_{(+)}^d + \Sigma_S^{0,\ H^+} \tag{10}$$

$$\Sigma_S^{\infty} = \beta_{(+)}^S e\Gamma_{(+)}^{S0} \tag{11}$$

where $\Sigma_S^{0,\ H^+}$ is the contribution to the DC specific surface conductivity from the protons of the water adsorbed onto the grain surface, $\beta_{(+)}^S$ is the mobility of counterions (e.g. Na^+) in the Stern layer (in $m^2/(sV)$), e is the elementary charge (e = 1.602×10^{-19} C), $\Gamma_{(+)}^d$ and $\Gamma_{(+)}^{S0}$ are the surface site densities (in counterions/m^2) of counterions in the diffuse and Stern layers, respectively, in the equilibrium state.

2.2 Complex conductivity of unsaturated porous media

The electrical properties (e.g., conductivity and permittivity) of hydrocarbon-bearing porous media were investigated extensively for the purpose of geophysical explorations. However, up to now, studies on hydrate-bearing porous media have been limited to either the bulk conductivity (neglecting the effects of the surface conductivity) or the high-frequency (e.g., the microwave frequency range, ~ GHz) permittivity (Spangenberg, 2001; Lee et al., 2008, 2010a). Gaining more understanding of the hydrate occurrence habits (in terms of the macro and micro-scale morphologies) and effects of the hydrate amount on the

resistivity/conductivity and saturation exponent in the Archie's equations is important. As a result, Spangenberg (2001) constructed idealized cubic-sphere-pack models that account for different morphologies such as the hydrate disseminated as a pore-filling material or a grain cement and as pure aggregations (e.g., nodules and layers). It was concluded that the saturation exponent was dependent on the sediment properties and on the saturation itself, and thus the use of a constant mean value for the saturation exponent could result in inaccurate estimation of the hydrate saturation (dented as s_h). Analysis of the experimental data for the non-cementation (i.e., pore-filling) morphology of hydrates (Spangenberg and Kulenkampff, 2006) supported the results from the theoretical modelling (Spangenberg, 2001) that the saturation exponent strongly first increased. It then reached a maximum, and then decreased with the increase of the water saturation (denoted as s_w). Lee et al. (2010a) performed laboratory measurements of the permittivity and conductivity of hydrate-bearing sediments in the frequency range of 0.2-1.3 GHz. It was shown that the permittivity combined with the complex refractive index model (CRIM) could provide reliable predictions of the free-water volume fraction and hydrate saturation in the absence of a gas phase in the pore space. It was also shown that the conductivity might be less reliable for estimating the hydrate saturation due to the uncertainty in the parameters of the Archie-type models and the ignorance of the surface conduction effects.

It should be noted that the relative permittivity of hydrates depends on the frequency of the applied electric field, e.g., $\varepsilon' > 60$ below 1 kHz and $\varepsilon' < 5$ above 100 MHz at a temperature higher than 0 °C for the tetrahydrofuran (THF) and methane hydrates (Lee, et al., 2007; Waite et al. 2009; Haukalid et al., 2017; Liu et al., 2020). The relative permittivity of hydrates in the low and high frequency ranges is associated with the rotational relaxation of water molecules in the lattice and the rotation of the encaged guest molecules (Hawkins and Davidson, 1966). Little is known about the low-frequency (e.g., lower than 1 MHz related to the induced polarization) effective permittivity of hydrate-bearing porous media. It needs to be stressed that the surface conduction cannot be ignored in a high specific surface sediment with a low pore-fluid conductivity, thus it may prevail in the clayey sediments (Waxman and Smits, 1968; Cook and Waite, 2018), some permafrost hydrate formations, and when the pore water is freshening due to the dissociation of hydrates (Waite et al., 2009; Klein and Santamarina, 2003). The bound-water layer coating the grains has been

considered in the theoretical modelling and analysis of the experimental data (Spangenberg, 2001; Spangenberg and Kulenkampff, 2006). However, only the bulk electrical conductance mechanism was included. In this work, both the Ohmic electromigration (responsible for the bulk and surface conductance) and polarization processes are taken into consideration through an analysis of the low-frequency complex conductivity of hydrate-bearing porous media.

The complex conductivity of a water-saturated porous medium as presented in **Section 2.1** provides a baseline for that of a porous medium filled with the water/gas, water/oil, water/hydrate or even water/hydrate/gas. The low-frequency complex conductivity of an unsaturated porous medium with the water/gas and water/oil has been investigated theoretically and experimentally (Revil et al., 2007; Jougnot et al., 2010; Schmutz et al., 2010, 2012; Breede et al., 2012; Revil, 2013). Jougnot et al. (2010) considered a representative elementary volume (REV) of a clayey rock filled with two continuous and immiscible fluids, i.e., the water as a wetting fluid and the air as a non-wetting fluid. To account for the partial water saturation of the porous medium, the volumetric charge density of the diffuse layer at the water-saturation condition was divided by the value of s_w. A mechanistic model of the complex conductivity for unsaturated clay-rocks was proposed and tested against the experimental data on partially saturated core samples. It was shown that the model worked well in reproducing the complex conductivity behavior at high frequencies (>1 Hz) for the water saturations between 0.2 and 0.8. In a similar work conducted by Schmutz et al. (2010), a non-wetting oil was used instead of air and the effects of the oil saturation on the complex-conductivity responses of oil-bearing sands were investigated through laboratory experiments and mechanistic modeling. The model was developed based on a description of the EDL polarization at the grain/water interface. The Stern layer polarization was dominant in the frequency range from 1 mHz to 100 Hz, and the oil/water interface was assumed to be uncharged. The low-frequency complex conductivity of the unsaturated porous medium can be written as (Jougnot et al., 2010; Schmutz et al., 2010; Revil, 2013):

$$\sigma^* = \frac{1}{F}\left[s_w^n \sigma_w + (F-1)\sigma_{sus}^* \right] \tag{12}$$

where s_w (dimensionless) denotes the water saturation in the pore space, σ_w (in S/m) is the conductivity of the

pore water, and σ^{*}_{sus} (in S/m) is the complex surface conductivity due to the EDL at unsaturated conditions (The subscript '*us*' stands for 'unsaturated'.). The two terms in the brackets of Eq. (12) correspond to three electrical processes responsible for the complex conductivity response of the porous medium. These are the frequency-independent conduction in the pore water, frequency-independent conduction in the diffuse layer and frequency-dependent polarization and conduction in the Stern layer. The in-phase conductivity of the unsaturated porous medium, which describes the conduction processes in both the pore water and EDL, can be written as:

$$\sigma' = \frac{s_w^n}{F}\left(\sigma_w + \beta_{(+)}\frac{Q_v}{s_w}\right) \tag{13}$$

where Q_v (in C/m^3) denotes the total volumetric charge density corresponding to the excess charges (within the EDL) per unit volume of the pore water. The quadrature conductivity of the porous medium can be related to the imaginary component of the complex surface conductivity by Eqs. (14)-(16) (Niu et al., 2016a; Revil, 2012).

$$\sigma'' = \left(1 - \frac{1}{F}\right)\sigma''_{sus} \tag{14}$$

$$\sigma''_{sus} = s_w^{n-1}\frac{1}{F\phi}\beta^S_{(+)} f_{pc} Q_v \left(\frac{\phi}{1-\phi}\right) \tag{15}$$

or

$$\sigma''_{sus} = s_w^{n-1}\frac{S_{Sp}}{F\phi}\rho_s \beta^S_{(+)} f_{pc} Q_S \tag{16}$$

where S_{Sp} (in m^2/kg) denotes the specific surface area, Q_S (in C/m^2) is the charge density of the grain surface, ρ_s (in kg/m^3) is the mass density of the grains, $\beta^S_{(+)}$ (in m^2/(sV)) is the mobility of the counterions in the Stern layer, and f_{pc} (dimensionless, called the partition coefficient) is the relative fraction of the counterions in the Stern layer controlled by the fluid chemistry and the mineralogy of the porous medium. The term $\beta^S_{(+)} f_{pc} Q_S$ in

Eq. (16) changes with the variations of the electrochemical properties of the interface between the pore water and solid grains, while the term $S_{Sp}/F\phi$ describes the geometry of the pores and skeleton of the porous medium.

2.3 Micro-distribution of hydrates in porous media

The micro-distribution modes are described based on the pore-scale spatial location of hydrates relative to the rock/sediment skeleton. Various groups of conceptional and idealized modes have been identified based on theoretical analysis, numerical simulations and direct observations on the cores from hydrate-bearing reservoirs or artificial samples. It can be found from the works reviewed in **Section 1** that different groups of micro-distribution modes of hydrates were adopted for investigating different types of physical properties of interest for hydrate-bearing porous media. The micro-distribution modes are elastic, hydraulic, thermal and electrical properties. It is reasonable because different physical properties have their own controlling factors. For instance, the electrical or hydraulic properties are controlled by the electrical current or the fluid-flow paths (only the electrical conduction mechanism is considered, but not the case in this work). Conversely, the elastic properties are controlled by the mechanical interactions between the hydrate and rock skeleton. Thus, the load bearing and bridging micro-distribution modes have often been dealt with separately when characterizing the elastic properties.

In this work, we focus on the electrical properties of hydrate-bearing porous media including both the conduction and polarization mechanisms. Special emphasis was given on the low-frequency complex conductivity related to the induced polarization. A hydrate-bearing porous medium consisting of the solid grains, pore water and hydrate can be obtained by replacing a part of the pore water with the hydrate in the original water-saturated porous-medium sample (Hyndman, et al., 1999). It has been shown in **Section 2.2** that the variations of the complex conductivity of oil or air-bearing porous media can be attributed to the change in the saturation or conductivity of the pore water, or the surface conductivity (i.e., the equivalent complex conductivity of grains in the mechanistic and numerical modeling approach). The existence of the hydrate in the pores results in a reduction of the water saturation, and thus a change in both the in-phase and quadrature

conductivities. These are deduced from Eqs. (12)-(16). This is a similar scenario to that for the non-wetting oil-bearing porous media, because the hydrate has a very low conductivity like oil (Waite et al., 2009; Frane et al., 2011; Haukalid et al., 2017). Moreover, it is also possible for the hydrate with a direct contact to the grain surface (e.g., in the frame-building and cementation modes) to alter the surface state of the grains, and thus further affect the complex surface conductivity besides the influence induced by a decreasing saturation of the conductive phase (e.g., the water solution in the pores).

We classify the micro-distribution modes of hydrates in a porous medium into two typical categories namely, the fluid-suspending mode and grain-attaching mode. The schematic of the two idealized micro-distribution modes can be found in **Section 3.2**. For the fluid-suspending mode, the hydrate floats in the pore fluid without any contact with the grains (i.e., no interactions with the grain surface); while for the grain-attaching mode a part of the grain surface contacts with the hydrate directly. The two types of micro-distribution modes have distinct characteristics in terms of the effects on the grain–surface state, and thus the equivalent electrical properties of the grains (i.e., complex surface conductivity). Presumably the complex surface conductivity is influenced by the hydrate in a more complicated way in the grain-attaching mode than that in the fluid-suspending mode. To summarize, we theorize that the complex conductivity of the hydrate-bearing porous medium is affected by both the micro-distribution mode and saturation of the hydrate.

3 Pore-scale numerical modelling

3.1 Modelling scheme

The numerical model is developed in order to obtain the complex conductivity responses of hydrate-bearing porous media. There are some issues to be addressed beforehand. These are: how to construct the skeleton of the porous medium, how to simulate the hydrate in the pore space, how to define the electrical properties (i.e., conductivity and dielectric constant) for each component (the grains, hydrate and water), and how to solve the model equations to obtain the electrical parameters of interest.

In this work, we constructed 2D geometries for the porous media skeletons. The grains were represented by

uniformly distributed circular ‘grains’ of the same size as shown in **Fig. 1**. Circular surfaces were utilized to represent the hydrate clusters in the fluid-suspending mode, while for the grain-attaching mode a geometric Boolean operation was adopted on the overlapped circular surfaces representing the grains and hydrate clusters. The grain phase itself has a negligible conductivity and dielectric constant, however, in the numerical modelling, the effects of the EDL coating on the grains were accounted for by combining the properties of the grains and EDL. The effective electrical parameters were assigned to the grain phase according to Eqs. (5) and (12).

The finite element method was adopted to solve the model equations of the electrical field, and then the complex conductivity was derived for the hydrate-bearing porous media modelled numerically. The commercial solver COMSOL Multiphysics (v5.5) accompanied with the AC/DC module was used to achieve the numerical modelling scheme.

3.2 Construction of computational domains

Two-dimensional geometries, with the same grain diameter and porosity to an objective porous medium, were constructed in the numerical modelling campaign. To validate the model solutions the same grain size with that reported in the literature (Leroy et al., 2008) was adopted. **Fig. 1** shows the computational domains including three phases, i.e., the solid grains, hydrate and pore water, with the hydrate in the fluid-suspending mode and grain-attaching mode, respectively.

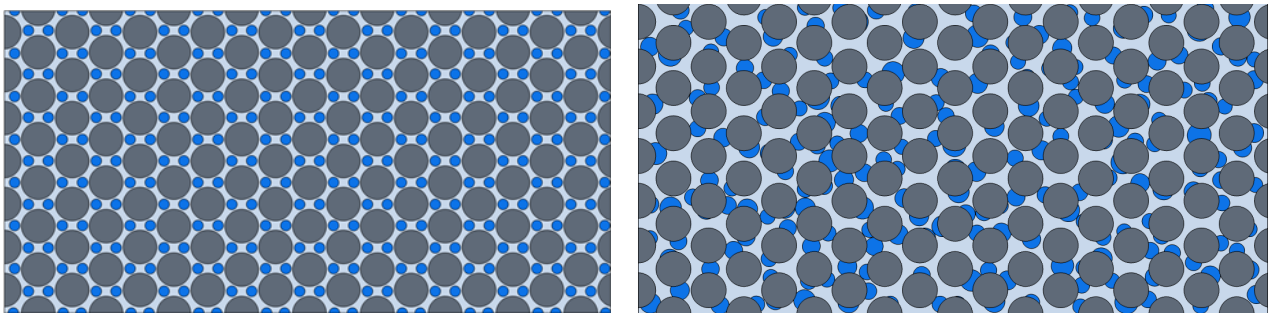

(a) Hydrate in the fluid-suspending mode (b) Hydrate in the grain-attaching mode

Fig. 1 Computational domains of the numerical models for different micro-distribution modes of hydrates (Blue: Hydrate cluster, Dark gray: solid grain, Light gray: pore water)

The 2D rectangular geometry with a length of 6.750 mm and width of 3.375 mm was constructed, in which 142 circles representing the outlines of grains with an diameter of 375 μm. The circles were allocated in the rectangular zone evenly, and a porosity of 0.40 was obtained at the no hydrate condition.

Hydrate clusters were generated artificially with constraints such as the hydrate saturation, diameter range of the circular surfaces representing hydrates and spatial distribution in the void space (including the pores and throats) of the simulated porous medium. For the fluid-suspending mode, circular surfaces representing hydrates without any contact to the grains were allocated in the void space. Different hydrate saturations were achieved by adjusting the range of diameters (including a specific case with only one diameter) of the circles. Both the pores and throats were occupied by hydrate clusters at high saturations (e.g., 0.5). For the grain-attaching mode, the hydrate clusters were represented by the sections of the raw circular surfaces, the diameter range of which were under control, excluding the overlap sections of the grains and raw circular surfaces. Different hydrate saturations were obtained by varying either the diameter range or the count of the raw circular surfaces for each diameter.

3.3 Materials and physical properties

In the computation domain for the representative elementary volume (REV) of a hydrate-bearing porous medium, there are three components or phases. These are the solid grains, water and hydrate. Therefore, three types of materials were defined in the numerical model. Because a current-conservation equation for the electrical field was solved in the models, the electrical properties of these materials were specified, i.e., conductivity and dielectric constant. It should be noted that the effective electrical properties of the solid grains were affected by several factors such as the frequency, salinity and saturation of the pore water, while those of the water and hydrate were assumed to be unchanged in the numerical model for a specified salinity and temperature.

The hydrate was assumed to be an electrical insulator and the dielectric constant was specified as 60 (Waite et al. 2009; Frane et al., 2011; Haukalid et al., 2017) at the frequency range involved in this work. An effective

conductivity (σ_{eff}) and dielectric constant (ε_{eff}) of the solid grains were computed by Eq. (17) with reference to Eq. (3), accounting for the complex-valued surface conductivity. The conductivity of the pore water was calculated by Eq. (18) to account for the temperature influence (Sen and Goode, 1992), and the dielectric constant was assigned to be a constant (i.e., 80). The effective dielectric constant of the solid grains due to the EDL-polarization was much higher (as shown in **Section 4.2**) than those of the water and hydrate, thus the dielectric constants for the water and hydrate were kept unchanged in the modelling.

$$\begin{cases} \sigma_{\text{eff}} = \sigma_s^{'} \\ \varepsilon_{\text{eff}} = \sigma_s^{''} / \omega \varepsilon_0 \end{cases} \tag{17}$$

$$\sigma_w = \left(5.6 + 0.27T - 1.5\times10^{-4}T^2\right)C_f - \left(\frac{2.36 + 0.099T}{1.0 + 0.214C_f}\right)\left(C_f\right)^{1.5} \tag{18}$$

where σ_w (in S/m) is the conductivity of the pore water, T (in ℃) denotes the temperature and C_f (in mol/L) is the salinity of the pore water.

3.4 Model equations and boundary conditions

The electric-field parameters of the computational domain constructed in **Section 3.2** were computed by utilizing the AC/DC module. The Electric Currents Interface of the module was adopted to compute the electric-field intensity, current and potential distributions in the computational domain, under the conditions where the inductive effects were negligible. The capacitive effects could be accounted for in the time (used in this work) and frequency domains.

A current-conservation equation based on the Ohm's law together with the constitutive relations (Eq. 19) was solved with the scalar electric potential as the dependent variable.

$$\begin{cases} \nabla \cdot \mathbf{J} = Q_{j,V} \\ \mathbf{J} = \sigma \mathbf{E} + \dfrac{\partial \mathbf{D}}{\partial t} + \mathbf{J}_{\mathbf{e}} \\ \mathbf{E} = -\nabla V \end{cases} \tag{19}$$

where $Q_{j,V}$ is the current source and $\mathbf{J}_e$ is the externally generated current density, which were set to be zero by default.

The types of interior and exterior boundary conditions were specified for the computational domain. The boundary condition at the interfaces between the three components, such as the solid grain, water, and hydrate, is continuity; that is

$$\mathbf{n} \cdot \left(\mathbf{J}_1 - \mathbf{J}_2 \right) = 0 \tag{20}$$

where **n** refers to the normal to the interface between any two components. Two opposite edges (the shorter ones) of the rectangular computational domain were specified as the ground and electrical potential boundaries, respectively. The remaining two edges were specified as the electric-insulation boundary. At the electric-insulation boundary, no electric current flows into the boundary; that is

$$\mathbf{n} \cdot \mathbf{J} = 0 \tag{21}$$

3.5 Meshing and solution scheme

The whole computation domain including the solid grains, water and hydrate was discretized with triangular elements. The mesh dependency of the numerical solution was examined, and then an appropriate level of mesh size was selected as detailed in **Section 4.1**. To conduct the numerical experiment for the mesh-dependence examination, a series of levels of mesh sizes were adopted. The mesh parameters used for the mesh dependence examination are listed in **Table 1**.

Table 1 Parameters of meshes for the mesh dependence examination

	Number of elements	Maximum size of elements (mm)	Minimum size of elements (mm)
1	8333	8.78×10^{-1}	4.05×10^{-2}
2	12729	6.75×10^{-1}	1.35×10^{-2}
3	25697	4.52×10^{-1}	2.03×10^{-3}
4	39286	1.00×10^{-1}	5.06×10^{-4}
5	94408	2.90×10^{-2}	6.75×10^{-3}
6	209326	1.87×10^{-2}	6.75×10^{-3}
7	324830	1.50×10^{-2}	6.75×10^{-3}
8	509351	1.20×10^{-2}	6.75×10^{-3}
9	743653	1.00×10^{-2}	6.75×10^{-3}

10	1135926	8.00×10^{-3}	6.75×10^{-3}
11	1496360	7.00×10^{-3}	6.75×10^{-3}
12	2025461	6.00×10^{-3}	3.75×10^{-3}

The electric current was obtained as a result of applying a sinusoidal voltage on the electric-potential boundary in the numerical model. A parametric sweep method was adopted with the frequency of the sinusoidal voltage ranging from 1×10^{-5} Hz to 1×10^{3} Hz. Both the electrochemical polarization mechanisms, corresponding to the EDL and MW polarization responses, were obtained from the numerical solution. To find the solution to this dynamic problem, the time-dependent solver with an implicit time-stepping method BDF (Backward differentiation formulas) was used for solving the differential equations of the physical models as presented in **Section 3.4**. The iterative linear-system solver using the conjugate gradient method was selected because less memory was required than the direct solver, and the relative tolerance could be adjusted flexibly. Finally, the complex conductivity of the REV of the simulated porous medium was derived from the numerical solutions under different conditions of interest.

4 Results

4.1 Mesh selection and model validation

A benchmark case that the REV was fully saturated with water was simulated numerically at different levels of meshes as presented in **Table 1**. Then the mesh dependence of the resultant complex conductivity was examined, based on which an appropriate level of mesh size was selected for further studies. **Fig. 2** shows the variations of the complex conductivity with the number of elements for different levels of meshes. Both the in-phase and quadrature conductivities converge to stable values gradually with the refinement of the mesh. Considering a tradeoff of the solution accuracy and computational effort, a mesh comprising of 743653 elements was selected and used in the numerical models throughout this work. The maximum and minimum sizes of the elements of the selected mesh are 6.75 μm and 10 μm, respectively.

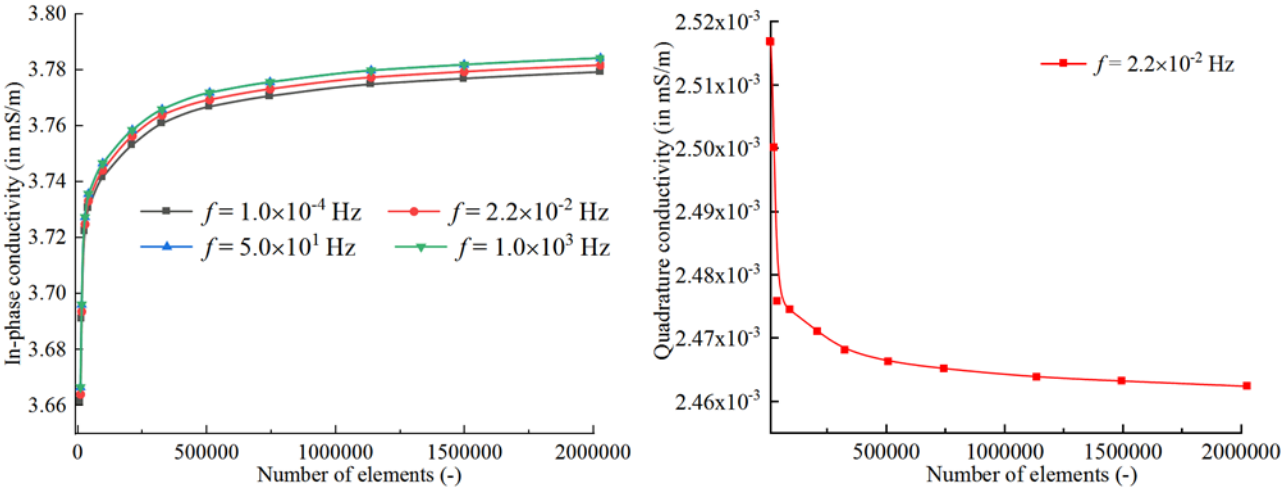

(a) In-phase conductivity (b) Quadrature conductivity

Fig 2 Variations of the complex conductivity with the number of elements for different mesh sizes

To validate the proposed numerical model two specific cases were computed numerically. The solutions were compared against results from the differential effective medium (DEM) theory and other models in the literature. The conditions (such as the geometry, pore-water and grain properties) of the first case were identical to those used by Niu and Zhang (2017) and Leroy et al. (2008), and the high salinity of the pore water in the second case guaranteed the applicability of the Archie's model. For the first case, the phase angle of the complex conductivity was compared with the solution from the model based on the DEM theory (Niu and Zhang, 2017) and that from the model proposed by Leroy et al. (2008) in **Fig.3**. It is seen that the numerical model proposed in this work reproduces the solution of the DEM model and the model of Leroy et al. (2008) well. The first peak in the lower frequency range can be identified in the frequency-dispersion spectrum of the phase angle clearly, which corresponds to the electrochemical polarization of the Stern layer coating on the grains. The frequency at which the phase angle reaches the maximum is denoted as the peak frequency and can be calculated by $f_{peak} = \frac{1}{2\pi\tau_0} \approx 22.2$ mHz. For the second case, a numerical simulation was conducted with the pore water of a high salinity (σ_w = 1.23 S/m), at which the contribution of the surface conductivity to the in-phase conductivity of the REV could be ignored safely. The Archie's parameters F, m and n for the REV were then derived from the model solutions. The fitted values of F, m and n are 3.936,

1.495 and 1.690, respectively. The fitted cementation exponent (m) from the solutions of the numerical model is very close to the theoretical value (m = 1.5) according to the DEM theory, showing again that the simple 2D model is a great analogue to the real case.

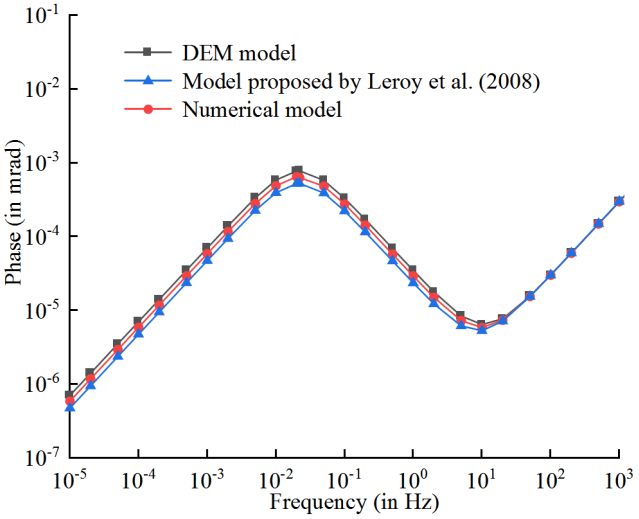

Fig. 3 Comparison of the phase angle spectra of the complex conductivity from the numerical model in this work, the differential effective medium (DEM) model and the model proposed by Leroy et al. (2008)

4.2 Effects of hydrate saturation

The complex conductivity of hydrate-bearing porous media at different saturations has been obtained from the solutions of the numerical model. The effects of hydrate saturation on complex conductivity have been examined with a reference to the theoretical model in **Section 2.2**. A series of hydrate saturations ranging from 0 to 0.5 has been simulated based on the approach presented in **Section 3.2**. The influences of the pore-fluid salinity and the hydrate micro-distribution are examined in **Section 4.3 and 4.4**, Hence, only the fluid-suspending mode and a constant salinity (i.e., 2×10^{-3} mol/L and 1.31×10^{-2} S/m) are analyzed in this section.

Both the in-phase and quadrature components of complex conductivity are affected by the hydrate saturation according to Eqs. (13)-(16). The frequency dispersion spectra of the complex conductivity parameters at different hydrate or water saturations (s_h = 1-s_w) are presented in **Fig. 4.** The conductivity parameters are

in-phase conductivity, quadrature conductivity, and phase angle. It can be observed that the first peaks of the quadrature conductivity and phase angle show up at the lower frequency section. Both the peaks of the quadrature conductivity and phase angle correspond to the polarization of the EDL coating on the grains. The peak frequency corresponds to the characteristic relaxation time of the polarization process. Generally, both the in-phase and quadrature conductivities decrease but the phase angle increases with increase in hydrate saturation. The in-phase conductivity decreases mainly due to a shrinkage of the conduction path in the pore fluid, because the hydrate acts as an insulating material in the background conductive fluid in the pores. It has been shown in Eqs. (12)-(16) that the volumetric charge densities of the Stern layer and diffuse layer for the water-saturated case is divided by s_w to account for the increase of the total charge densities (Q_v) with a decreasing s_w (i.e., an increasing s_h). Moreover, the effects on the shrinkage of the cross-sectional area of the conduction path is taken into account by introducing a multiplication factor s_w^n.

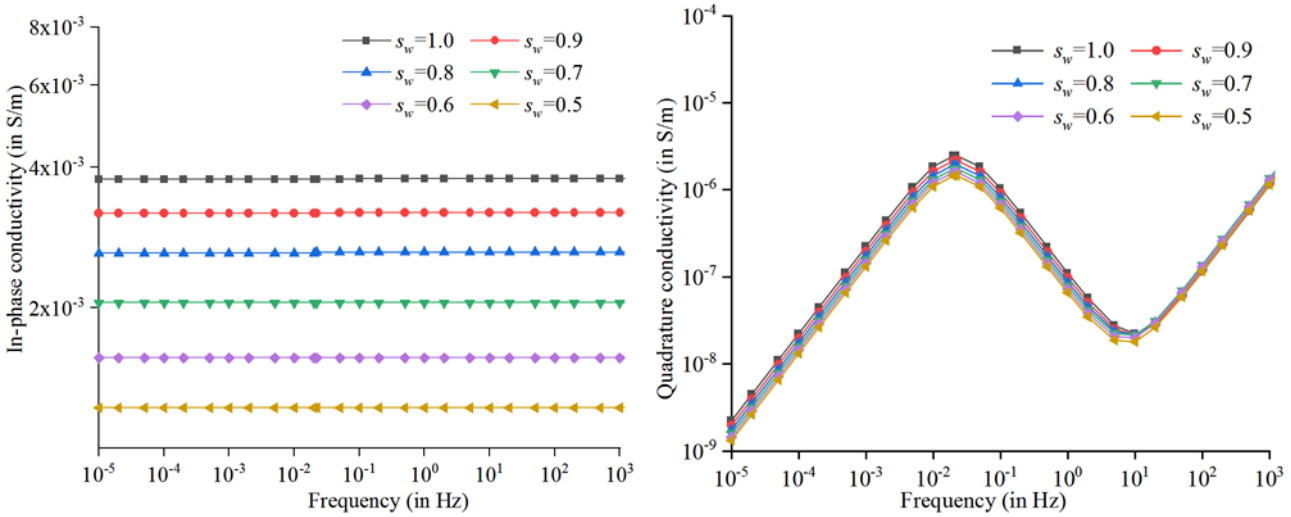

(a) Frequency-dispersion spectra of in-phase conductivity (b) Frequency-dispersion spectra of quarature conductivity

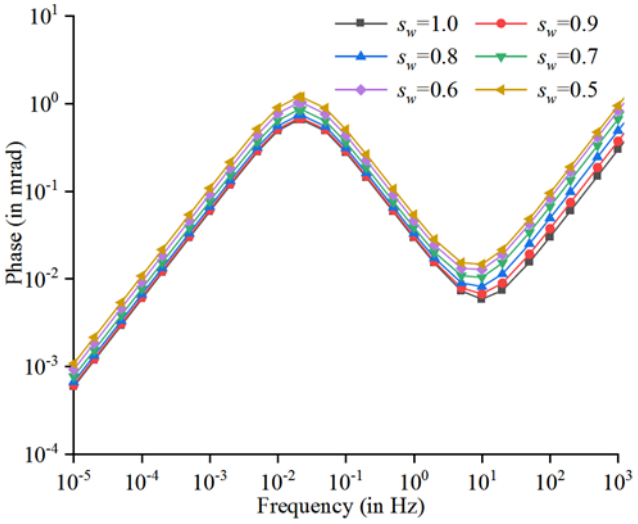

(c) Frequency-dispersion spectra of phase angle

Fig 4 Frequency-dispersion spectra of the complex conductivity parameters at different water/hydrate saturations

The in-phase conductivity and quadrature conductivity at the peak frequency are correlated with the water saturation based on the power-law relationships (i.e., Eqs. (22) and (23)), respectively. It can be seen in **Fig. 5** that the complex conductivity can be fitted very well by power law relationships as indicated by the high R-squared values, such as 0.997 and 0.972. It also shows that the numerical model reproduces the theoretical model predictions successfully. For the in-phase conductivity, the fitted saturation exponent and in-phase conductivity for the water-saturated case are 1.70 and 3.78 mS/m, respectively. These values are consistent with those (n = 1.690 and $\sigma'_{(s_w=1.0)}$ = 3.77 mS/m) from Archie's model and the model of Leroy et al. (2008).

For the quadrature conductivity, the fitted saturation exponent follows $p = n_c - 0.922$, which is consistent with the relationship $p = n - 1$ in the model of Revil (2013). The quadrature conductivity for the water-saturated case is fitted to be 2.38×10^{-3} mS/m, which deviates from the Revil's model ($\sigma''_{(s_w=1.0)}$ = 2.47×10^{-3} mS/m) by 3.6 %.

$$\sigma'(s_w) = \sigma'_{(s_w=1.0)} s_w^{n_c} \tag{22}$$

$$\sigma''(s_w) = \sigma''_{(s_w=1.0)} s_w^{p} \tag{23}$$

To demonstrate the significant effects of the EDL polarization in the low frequency range (i.e., lower than 1 kHz), the quadrature conductivity is then converted into the effective dielectric constant (ε_{eff}) according to Eqs. (3) and (17). As shown in **Fig. 6,** an effective dielectric constant in the order of 10^6 shows up in the frequency range lower than the peak frequency, then it drops dramatically with the increase of the frequency. The relationship between ε_{eff} at the peak frequency and s_w are modelled based on both the power law and linear regression approach.

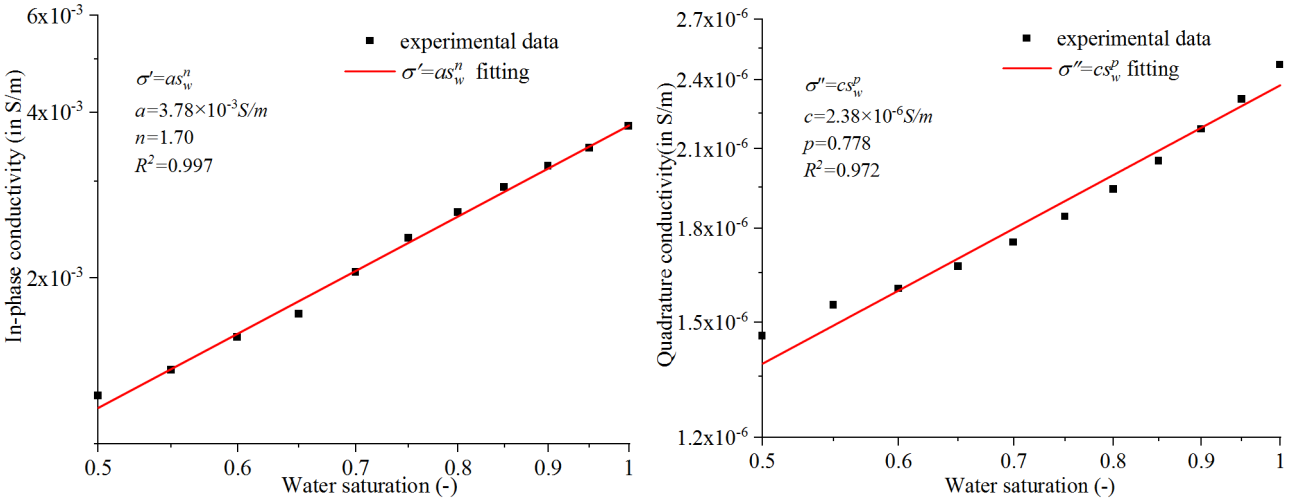

(a) In-phase conductivity with water saturation (b) Quadrature conductivity with water saturation

Fig. 5 Correlations between parameters of the complex conductivity at the peak frequency and water saturation

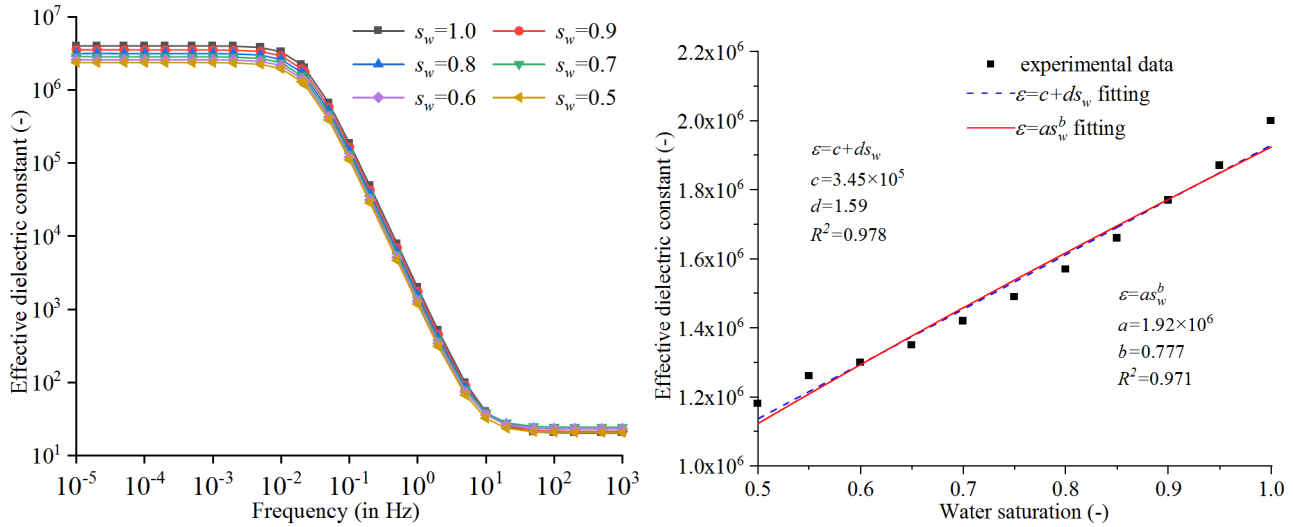

(a) Frequency-dispersion spectra (b) Correlations

Fig. 6 Frequency-dispersion spectra of the effective dielectric constant and correlations between the

effective dielectric constant at the peak frequency and water saturation

4.3 Effects of pore-fluid salinity

The salinity of the pore fluid affects both the in-phase and quadrature conductivities of the complex conductivity of porous media (Revil and Skold, 2011; Revil, 2012; Niu et al., 2016b). The salinity effects on the complex conductivity of hydrate-bearing porous media have been investigated by using the numerical model. A series of salinities ranging from 2×10^{-4} mol/L to 3 mol/L were assigned to the pore water in the model corresponding to a conductivity range from 1.33×10^{-3} S/m to 11.3 S/m. The complex conductivity was subsequently aobtained from the numerical solutions. Typical cases with the hydrate saturations of 0.25 and 0.50 in the fluid-suspending mode are analyzed below.

It has been demonstrated by Revil and Skold (2011) that the specific surface conductivity of the Stern layer increases with the pore fluid salinity due to increase in the number of counterions adsorbed into the Stern layer. Furthermore, the quadrature conductivity of sands and sandstones increases with the conductivity of the NaCl solution and becomes independent of the salinity above 1 S/m. The dependency of the specific surface conductivity of the Stern layer can be expressed as Eq. (24).

$$\Sigma_S = \beta_{\mathrm{Na}^+}^S e\Gamma_S^0 \left(\frac{K_{\mathrm{Na}} C_f}{K_{(-)} + 10^{-\mathrm{pH}} + K_{\mathrm{Na}} C_f} \right) \tag{24}$$

where $\beta_{\mathrm{Na}^+}^S$ (in $m^2/(sV)$) is the mobility of the counterions Na^+ in the Stern layer, Γ_S^0 (in counterions/m^2) is the total site density at the surface of the grain, K_{Na} and $K_{(-)}$ (dimensionless) denote the sorption coefficient for Na^+ and H^+, respectively, C_f (in mol/L) is the salinity of the pore fluid.

The variations of the quadrature conductivity of hydrate-bearing porous media with frequency and the quadrature conductivity at the peak frequency with the salinity are shown in **Fig. 7**. It can be observed that the quadrature conductivity increases with an increase in the pore-water salinity at the same hydrate saturation. In

the low-salinity range (lower than 0.1 S/m), the quadrature conductivity increases sharply with increasing pore-fluid conductivity. Subsequently, the growth rate drops in the intermediate-salinity range (between 0.1 S/m and 1.0 S/m). Finally, the quadrature conductivity becomes almost independent of salinity when the pore-water conductivity is over 1.0 S/m. This is consistent with the experimental measurements reported by Revil and Skold (2011). That the quadrature conductivity is independent of the pore-water salinity is quite favorable for predicting the hydrate saturation based on the quadrature conductivity of the porous medium. The stability of the gas hydrate is prone to environmental conditions such as pressure and temperature. It often happens that a part of the hydrate in the porous medium dissociates into gas and water. New hydrates may re-form to respond to the variations of pressure and temperature around the phase equilibrium point of the hydrate. In these dynamic processes, the salinity of the pore water becomes frequently variable and unpredictable. This is because the salinity decreases with hydrate dissociation due to pore water release and increases with hydrate formation due to the salt-exclusion effect. The unpredictable salinity of the pore water poses the challenge of estimating the hydrate saturation based on the in-phase conductivity. But it is not the case for the quadrature conductivity, because the quadrature conductivity is immune to the change of the pore water conductivity at high salinities as shown in **Fig. 7**.

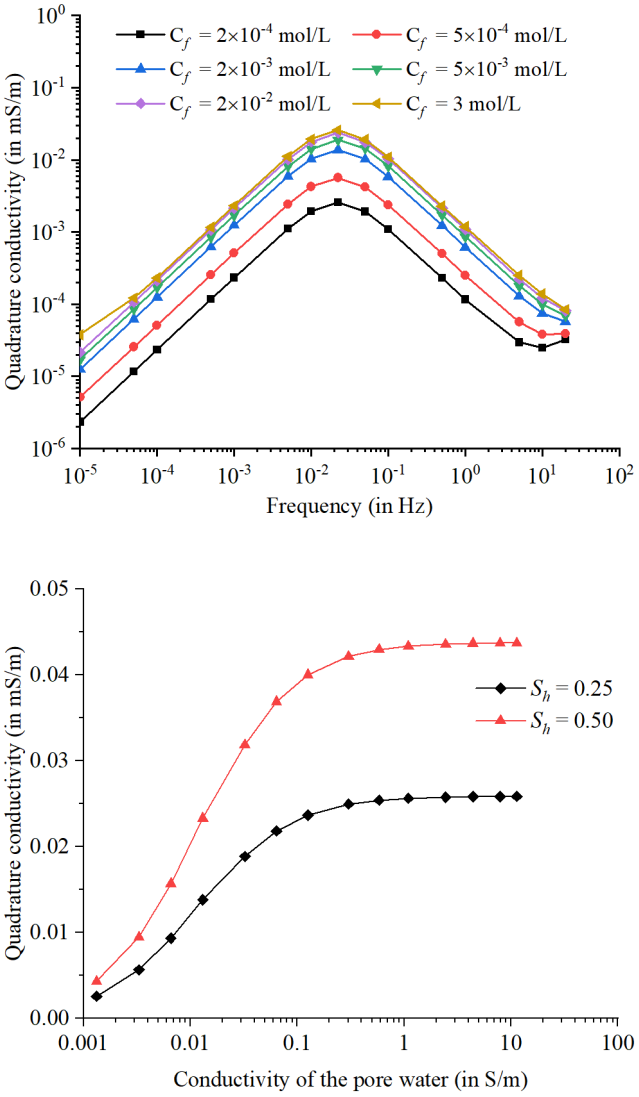

(a) Spectra of quadrature conductivity for S_h = 0.25 (b) Quadrature conductivity at the peak frequency

Fig. 7 Frequency-dispersion spectra of the quadrature conductivity (S_h = 0.25) and the quadrature conductivity at the peak frequency at different salinities of the pore water

To account for the effects of both the hydrate saturation and pore-water salinity, the quadrature conductivity of the hydrate-bearing porous medium at various saturations and three salinities (i.e., 1.10 S/m, 4.41 S/m and 11.30 S/m) were computed with the numerical model. **Fig. 8** shows the relationship between the quadrature conductivity at the peak frequency and hydrate saturation with the pore-water conductivities above 1.0 S/m. It can be seen in **Fig. 8** that the quadrature conductivities for the three salinities are close to each other under the high salinity conditions as expected. The relationships between the quadrature conductivity and hydrate saturation have been fitted separately and then together for the three cases. A power law relationship was used

and the saturation exponents were derived. Compared with the low salinity case presented in **Section 4.2**, the saturation exponent reaches a stable value around 0.805 when the pore water conductivity exceeds 1.0 S/m.

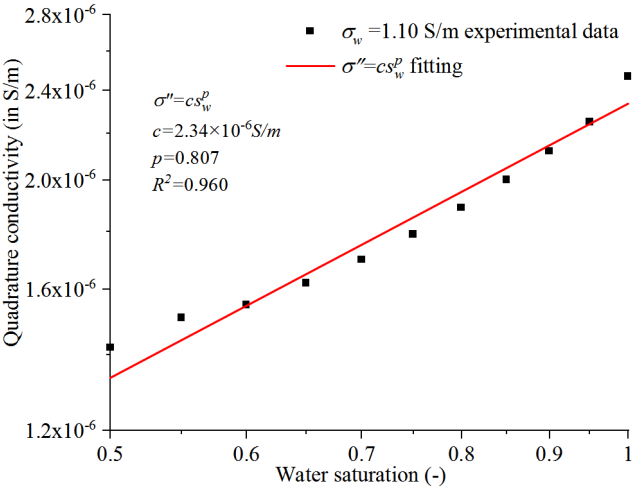

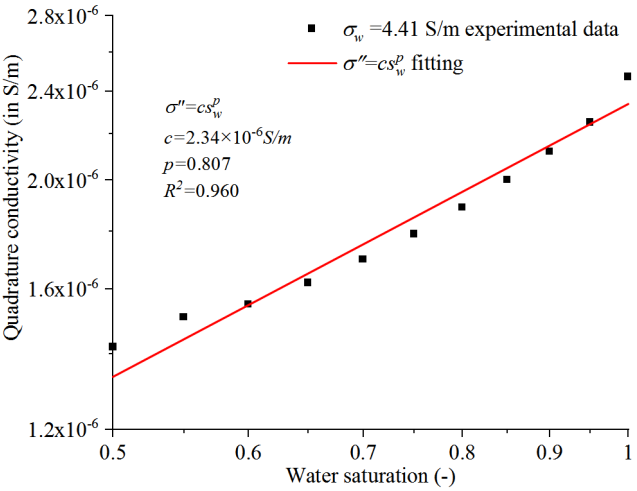

(a) σ_w = 1.10 S/m (b) σ_w = 4.41 S/m

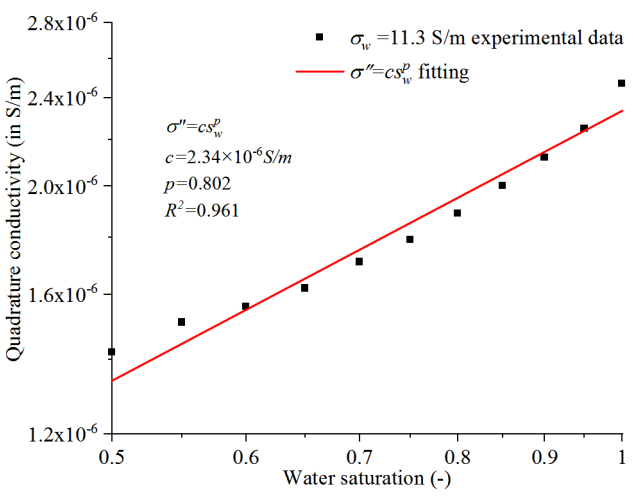

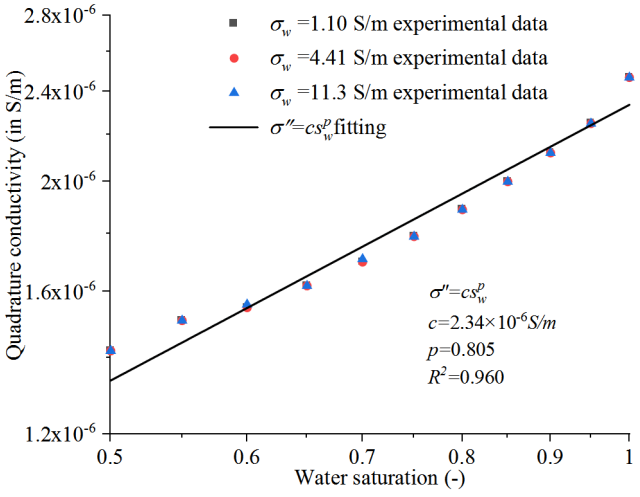

(c) σ_w = 11.30 S/m (d) σ_w = 1.10 S/m, 4.40 S/m, 11.30 S/m

Fig. 8 Correlations between the quadrature conductivity and water saturation at high salinities of the pore water

4.4 Effects of hydrate micro-distribution

Both the hydrates fluid-suspending (in **Section 4.2 and 4.3**) and grain-attaching modes have been simulated with the numerical model. The effects of the hydrate micro-distribution mode were investigated through an analysis of the complex conductivity of hydrate-bearing porous media at the same saturations and salinities. It needs to be mentioned that the analysis was limited to the effects of the micro-distribution mode on the in-phase conductivity below. The mechanism of the effects on the quadrature conductivity is much more complicated and not clear currently, thus it deserves a dedicated work to demonstrate the effects of the hydrate micro-distribution, understand the underlying mechanisms and develop an effective and efficient modelling approach in the future.

The in-phase conductivity includes the contribution from both the pore water and grain surface coated by the EDL. In this work, we theorize that the contact between the hydrate and grain surface leads to a decrease in the specific surface area and thus a shrinkage of the EDL. We define a correction factor $\left(1-f_{Sp}\right)$ as shown in Eq. (25) to describe the reduction of the specific surface area and blockage to the surface conduction path to account for EDL shrinkage.

$$1-f_{Sp}=\frac{S_{Spc}}{S_{Sp}} \tag{25}$$

where S_{Spc} denotes the grain surface area coated by the hydrate in terms of the specific surface area. Therefore, Eqs. (13) and (16) can be corrected and then rewritten as

$$\sigma'=\frac{s_w^n}{F}\left(\sigma_w+f_{Sp}\beta_{(+)}\frac{Q_v}{s_w}\right) \tag{26}$$

The contribution from the surface conduction decreases with an increase in the coated area on the grains by the hydrate as indicated by Eq (26). Furthermore, it can be neglected if the salinity of the pore water is relatively high, e.g., higher than 1×10^{-3} mol/L, which is common in the laboratory samples and the marine

hydrate sediments. Consequently, a change in the real component of the surface conductivity due to hydrate coating on the grains in the grain-attaching mode can be negligible safely at high salinities.

In this section, six typical cases for the two micro-distribution modes (i.e., the fluid-suspending and grain-attaching modes) were provided to analyzing the effects of hydrate distribution. The detailed parameters of the six cases are listed in **Table 1**. To ensure that the cases are comparable with each other, the same hydrate saturation of 0.3 was used as a mandatory constraint condition. In the cases denoted as Case 5 and Case 6 labeled as 'Random', the hydrate clusters represented by the circular surfaces of the same (Case 5) or five different diameters (Case 6) were allocated in the rectangular domain representing the simulated porous media (as shown in **Fig. 1**) in a random way. The first three cases (Cases 1 to 3) were designed to examine the effects of hydrate cluster diameter range and distribution in the rectangular domain for the fluid-suspending mode. A single diameter was used in Case 1 and five diameters were used in Cases 2 and 3. The diameters increased from the left to right and from the bottom and top for Case 2 and Case 3, respectively. The last three cases, i.e., Case 4, Case 5 and Case 6, correspond to the grain-attaching mode. Both Case 4 and Case 5 used a single diameter for hydrate clusters and the only difference is the distribution of hydrates in the rectangular domain. **Fig. 9** shows the frequency-dispersion spectra of the in-phase conductivity of hydrate-bearing porous media for typical cases at $s_h = 0.3$. Additionally, the spatial distributions of electrical current density are shown in **Fig. 10**.

Table 1 Parameters of the six cases

Case	Micro-distribution mode of hydrates in the void space	Regular or random distribution of hydrates in the domain	Diameters of hydrate clusters (μm)
1	Fluid-suspending	Regular	118
2	Fluid-suspending	Regular	104, 112, 118, 124, 130 (From left to right)
3	Fluid-suspending	Regular	104, 112, 118, 124, 130 (From bottom to top)
4	Grain-attaching	Regular	240
5	Grain-attaching	Random	240
6	Grain-attaching	Random	200, 220, 240, 260, 280

It can be observed in **Fig. 9** that lower in-phase conductivities are obtained from Case 5 and 6, which are characterized by a 'random' distribution of hydrate clusters for the grain-attaching mode. The in-phase

conductivity for Case 6 with a range of diameters for hydrate clusters is higher than that of Case 5. The cases characterized by a 'regular' distribution of hydrate clusters for either the fluid-suspending or grain-attaching modes present significantly higher in-phase conductivity. The in-phase conductivity of Case 1 and Case 4 are nearly the same, while that of Case 2 and Case 3 is slightly lower.

The variations of the in-phase conductivity of the six cases can be explained using an analysis of the characteristics of electrical conduction paths in the simulated porous media. The conduction paths are indicated by the current-density lines presented in **Fig. 10**. Essentially, the in-phase conductivity depends on the tortuosity of conduction paths of the electrical current for the six cases. A higher tortuosity of the conduction paths results in a lower in-phase conductivity. A blockage of the conduction paths is an extreme scenario that can significantly increase the tortuosity. For the grain-attaching mode, it is a common occurrence that the hydrate clusters block part of the electrical current conduction paths, hence lowering the in-phase conductivity of hydrate-bearing porous media. The blockage of the conduction paths can be clearly found in Cases 5 and 6, where the electrical current has to find a more tortuous flow path. For the fluid-suspending mode, there is no blockage to the conduction paths by the hydrate clusters as presented by Cases 1–3. Thus, no significant variations in the in-phase conductivity can be observed, because the hydrate saturation is the same (s_h = 0.3) for the three cases. The effects of the hydrate clusters in Cases 1–3 are analogous to resistors in an electrical circuit. The resistances correspond to hydrate cluster diameters within the pores or throats, and smaller diameters result in wider conduction paths and thus lower resistances. An electrical circuit with five resistors of the same resistance connected in parallel or in series can be an equivalent to Case 1. For Cases 2 and 3, five resistors of different resistances (corresponding to the five diameters) are needed, which are connected in series and in parallel for Case 2 and 3 respectively. Based on the basic theory of electrical circuits, the total resistance for Case 3 with a parallel connection is lower than that for Case 2 with a series connection. Thus the in-phase conductivity for Case 3 is higher than that for Case 2 as presented in **Fig. 9**. For the grain-attaching mode, there is a special case (Case 4) which has a much higher in-phase conductivity than the other two cases (Cases 5 and 6),. Case 4 is characterized by clear conduction paths without any blockage compared with Cases 5 and 6. In this sense, Case 4 is quite similar to cases in the suspending mode (Case

1–3). Therefore, it is not surprising that the in-phase conductivity of the four cases is quite close. Generally, it is not common that there is no blockage to the conduction paths in hydrate-bearing porous media for the grain-attaching mode. To summarize, the differences in the in-phase conductivity among the six cases at the same hydrate saturation emphasizes the necessity to account for the effects of the hydrate distribution in the porous media.

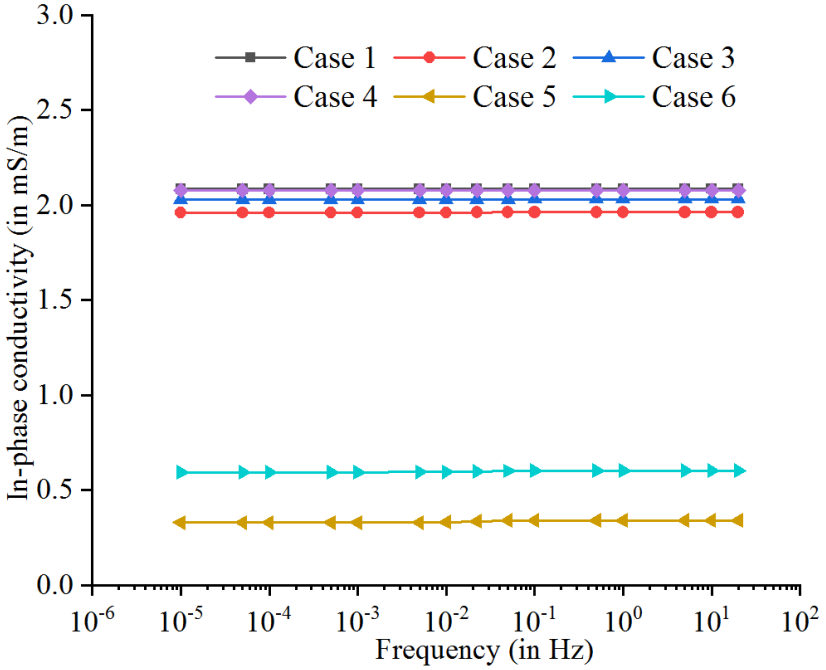

Fig. 9 Frequency-dispersion spectra of the in-phase conductivity for different micro-distribution modes of hydrates

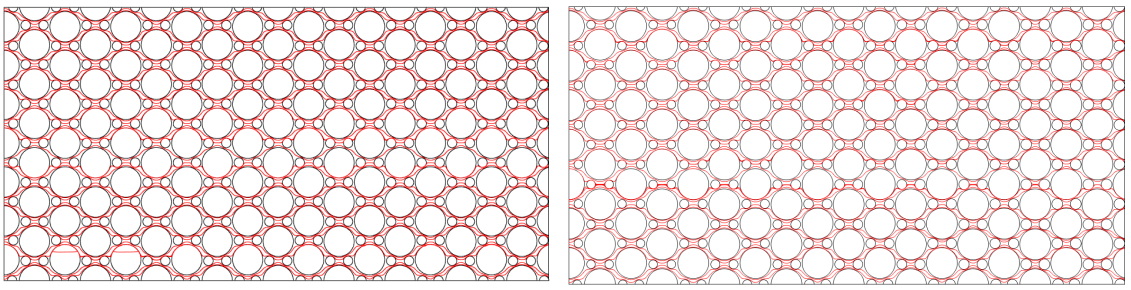

(a) Case 1 (b) Case 2

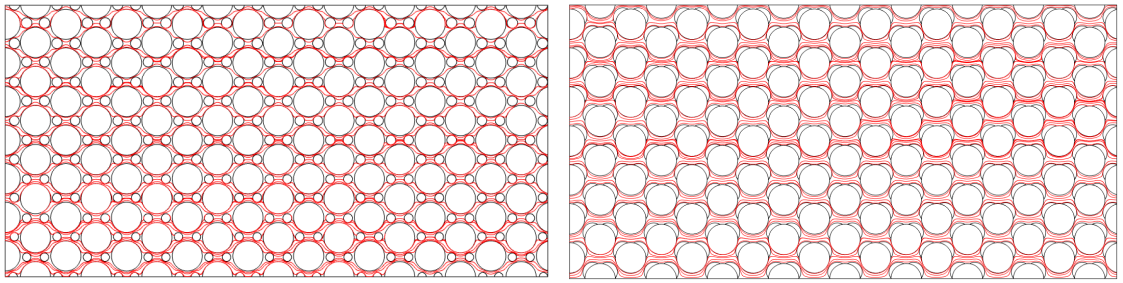

(c) Case 3 (d) Case 4

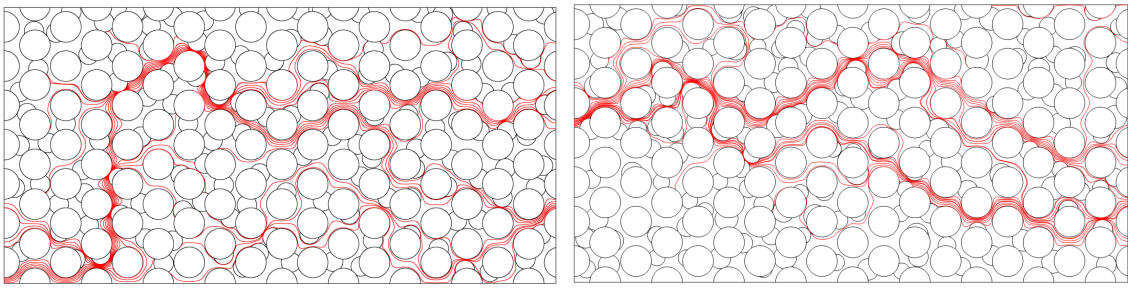

(c) Case 5 (d) Case 6

Fig. 10 Spatial distributions of the electrical current density for different micro-distribution modes of hydrates

5 Discussion

5.1 Model for hydrate-saturation evaluation

It has been demonstrated in **Section 4** that the hydrate saturation can be correlated with the real and imaginary components of the complex conductivity, i.e., the in-phase and quadrature conductivities of the porous media. The correlations can be considered as the hydrate-saturation evaluation models. However, there are some issues to be noted when utilizing these models in the real applications.

The in-phase conductivity of the hydrate-bearing porous medium depends not only on the hydrate saturation, but also on the salinity of the pore water. In the lower range of the pore water conductivity, (e.g., lower than 0.001 S/m), the relationship between the in-phase conductivity and pore-water conductivity in the log-log space exhibits a nonlinear behavior owing to the non-negligible role played by the surface conductivity. Certainly, Archie's model is applicable in the higher range of the pore water conductivity when the surface

conductivity can be safely neglected. Therefore, care must be taken when using the in-phase conductivity-based models for calculating the hydrate saturation in clayey marine sediments, where the surface conduction can be significantly enhanced by the clay.

The micro-distribution mode modifies the relationship between the quadrature conductivity and hydrate saturation. We note that the coated area of the grain surface by hydrates may vary significantly even at the same hydrate saturation. This issue poses difficulties to an establishment of a unified model for deriving the hydrate saturation from the quadrature conductivity of the porous medium alone. It implies that other parameters sensitive to the contact state between the hydrates and grains are required. These include the elastic wave velocity, elastic modulus and elastic wave attenuation (Lee et al., 2010b; Bu et al., 2019; Pan et al., 2020ab; Liu et al., 2020; Xing et al., 2020). In the work presented in this paper, the analysis and correlations have been limited to the electrical parameters.

5.2 Geometry for numerical modelling

A simple 2D geometry has been used extensively in this work to examine the effects of the hydrate saturation, salinity of the pore water and hydrate micro-distribution mode. To simulate the real 3D porous medium, the porosity and grain diameter have been adjusted according to the real case, but a Delta distribution of the grain size has been assumed for simplicity. The simplification of the model geometry and dimension possesses great advantages due to the reduced computational requirements and increased stability of the solutions. Furthermore, it retains the capability to simulate near real cases. The capability of the simplified 2D model was validated by comparing the numerical solutions and experimental measurements as well as with the theoretical models. However, at least two limitations can be identified when generalizing the applications of 2D numerical models. Firstly, the contact state between the ‘grains’ cannot be simulated with these models because a certain space between the grains must be set aside to achieve the prespecified porosity, as well as to allow the conduction current to form in the pore space. It is presumable that the tortuosity of the conduction current paths has not been simulated properly in the 2D model. Secondly, the surface conduction has been handled by applying a volume averaging approach to the spheres, and the resultant complex surface

conductivity is assigned to the 2D ‘grains’ in terms of an effective conductivity and dielectric constant. Essentially, the 2D ‘grains’ are treated as cylinders with the diameter of the cross-sections equal to that of the simulated 3D granular spheres. This may result in discrepancies between the 2D and 3D solutions. Therefore, considering the limitations stated above, future work should focus on constructing 3D numerical models for quantitatively evaluating the effects of model dimension on the tortuosity and surface conduction.

6 Conclusions

To investigate the complex conductivity of hydrate-bearing porous media and derive correlations between the hydrate saturation and complex conductivity, we have presented a pore-scale numerical approach for developing finite-element based models. The effects of the hydrate saturation, salinity of the pore fluid and hydrate micro-distribution mode on the frequency-dispersion spectra of the complex conductivity have been analyzed based on numerical model solutions. Correlations between the hydrate saturation and parameters of the complex conductivity of hydrate-bearing porous media taking account of the effects of the pore-fluid salinity and pore-scale micro-distribution, serving as potential models for evaluating the hydrate saturation, have been obtained.

(1) A simple 2D numerical model can capture the dominant characteristics of the complex conductivity of hydrate-bearing porous media. The model solutions are comparable to Archie’s model, the models of Revil and co-workers, as well as the differential effective medium model. The in-phase conductivity, quadrature conductivity and effective dielectric constant calculated from the numerical model solutions can be correlated with the hydrate saturation based on a power law relationship in the log-log space. Based on the correlations, the hydrate-saturation calculation methods can be derived.

(2) The relationship between the hydrate saturation and complex conductivity is affected by the pore-water salinity. However, a constant saturation exponent of the power-law correlation between the hydrate saturation and quadrature conductivity can be obtained when the pore-water conductivity exceeds 1.0 S/m. This correlation can be used as a hydrate saturation evaluation model even if the hydrate experiences stochastic

formation and dissociation processes. This is because the model is immune to the variation of the pore-water conductivity in the high-salinity zone.

(3) Two types of hydrate micro-distribution modes in porous media can be defined within the framework of the complex conductivity analysis. For the fluid-suspending mode, the hydrate floats in the pore fluid without any interaction with the grain surface. Conversely, for the grain-attaching mode, a part of the grain surface is coated with the hydrate. Although the saturation and salinity remain constant, the porous medium in-phase conductivity still varies due to the difference in the pore-scale distributions of hydrates, which is attributed to the change in the tortuosity of the electrical conduction paths.

Acknowledgement

The authors would like to express sincere thanks to the financial support by the Fundamental Research Funds for the Central Universities (20CX05005A and 18CX02112A), the Major Scientific and Technological Projects of CNPC (ZD2019-184-001), PetroChina Innovation Foundation (2018D-5007-0214), Shandong Provincial Natural Science Foundation (ZR2019MEE095, ZR2017BEE026) and National Natural Science Foundation of China (51306212, 41704124). Thanks for Dr. ?? for reading the …

References

Archie, G. E., 1942. The electrical resistivity log as an aid in determining some reservoir characteristics, *Transactions of the AIME*, 146(01), 54-62.

Boswell, R., Collett, T. S., 2011. Current perspectives on gas hydrate resources, *Energy & Environmental Science*, 4(4), 1206-1215.

Breede, K., Kemna, A., Esser, O., Zimmermann, E., Vereecken, H., Huisman, J. A., 2012. Spectral induced polarization measurements on variably saturated sand-clay mixtures, *Near Surface Geophysics*, 10(6),

479-489.

Bu, Q., Hu, G., Liu, C., Xing, T., Li, C., Meng, Q., 2019. Acoustic characteristics and micro-distribution prediction during hydrate dissociation in sediments from the south china sea. *Journal of Natural Gas Science and Engineering*, 65, 135-144.

Chen, X., Verma, R., Espinoza, D. N., Prodanović, M., 2018. Pore-scale determination of gas relative permeability in hydrate‐bearing sediments using X-ray computed micro‐tomography and lattice Boltzmann method, *Water Resources Research*, 54(1), 600-608.

Cook, A. E., Waite, W. F., 2018. Archie's saturation exponent for natural gas hydrate in coarse-grained reservoirs, *Journal of Geophysical Research: Solid Earth*, 123(3), 2069-2089.

Dai, S., Santamarina, J. C., Waite, W. F., Kneafsey, T. J., 2012. Hydrate morphology: Physical properties of sands with patchy hydrate saturation, *Journal of Geophysical Research: Solid Earth*, 117(B11), 1-12.

Dong, H., Sun, J., Lin, Z., Fang, H., Li, Y., Cui, L., Yan, W., 2018. 3D pore-type digital rock modeling of natural gas hydrate for permafrost and numerical simulation of electrical properties, *Journal of Geophysics and Engineering*, 15(1), 275-285.

Dong, H., Sun, J., Zhu, J., Liu, L., Lin, Z., Golsanami, N., Cui, L., Yan, W., 2019. Developing a new hydrate saturation calculation model for hydrate-bearing sediments, *Fuel*, 248, 27-37.

Du Frane, W. L., Stern, L. A., Weitemeyer, K. A., Constable, S., Pinkston, J. C., Roberts, J. J., 2011. Electrical properties of polycrystalline methane hydrate, *Geophysical Research Letters*, 38(9),1-5.

Dvorkin, J., Helgerud, M.B., Waite, W.F., Kirby, S.H., Nur, A., 2000. Introduction to physical properties and elasticity models. In: Max, M.D. (Ed.), Natural Gas Hydrate in Oceanic and Permafrost Environments. Kluwer, Dordrecht, 245-260.

Ersland, G., Husebø, J., Graue, A., Baldwin, B. A., Howard, J., Stevens, J., 2010. Measuring gas hydrate formation and exchange with CO_2 in Bentheim sandstone using MRI tomography, *Chemical Engineering Journal*, 158(1), 25-31.

Freedman, R., Vogiatzis, J. P., 1986. Theory of induced-polarization logging in a borehole, *Geophysics*, 51(9),

1830-1849.

Fukumoto, A., Kamada, K., Sato, T., Oyama, H., Torii, H., Kiyono, F., et al., 2018. Numerical simulation of pore-scale formation of methane hydrate in the sand sediment using the phase-field model, *Journal of Natural Gas Science and Engineering*, 50, 269-281.

Haukalid, K., Folgerø, K., Barth, T., Fjermestad, S. L., 2017. Hydrate formation in water-in-crude oil emulsions studied by broad-band permittivity measurements, *Energy & Fuels*, 31(4), 3793-3803.

Hawkins, R. E., Davidson, D. W., 1966. Dielectric relaxation in the clathrate hydrates of some cyclic ethers, *The Journal of Physical Chemistry*, 70(6), 1889-1894.

Hyndman, R. D., Yuan, T., Moran, K., 1999. The concentration of deep sea gas hydrates from downhole electrical resistivity logs and laboratory data, *Earth and Planetary Science Letters*, 172(1-2), 167-177.

Ishai, P. B., Talary, M. S., Caduff, A., Levy, E., Feldman, Y., 2013. Electrode polarization in dielectric measurements: a review, *Measurement science and technology*, 24(10), 102001-102021.

Jougnot, D., Ghorbani, A., Revil, A., Leroy, P., Cosenza, P., 2010. Spectral induced polarization of partially saturated clay-rocks: A mechanistic approach, *Geophysical Journal International*, 180(1), 210-224.

Kemna, A., Binley, A., Cassiani, G., Niederleithinger, E., Revil, A., Slater, L., et al., 2012. An overview of the spectral induced polarization method for near-surface applications, *Near Surface Geophysics*, 10(6), 453-468.

Kerkar, P., Jones, K. W., Kleinberg, R., Lindquist, W. B., Tomov, S., Feng, H., Mahajan, D., 2009. Direct observations of three dimensional growth of hydrates hosted in porous media, *Applied Physics Letters*, 95(2), 1-3.

Klein, K. A., Santamarina, J. C., 2003. Electrical conductivity in soils: Underlying phenomena, J*ournal of Environmental & Engineering Geophysics*, 8(4), 263-273.

Kneafsey, T. J., Seol, Y., Gupta, A., Tomutsa, L., 2011. Permeability of laboratory-formed methane-hydrate-bearing sand: measurements and observations using X-ray computed tomography, *SPE Journal*, 16(01), 78-94.

Kneafsey, T. J., Tomutsa, L., Moridis, G. J., Seol, Y., Freifeld, B. M., Taylor, C. E., Gupta, A., 2007. Methane

hydrate formation and dissociation in a partially saturated core-scale sand sample, *Journal of Petroleum Science and Engineering*, 56(1-3), 108-126.

Kou, X., Li, X. S., Wang, Y., Liu, J. W., Chen, Z. Y., 2021. Effects of gas occurrence pattern on distribution and morphology characteristics of gas hydrates in porous media. *Energy*, 226, 120401.

Lee, J. Y., Santamarina, J. C., Ruppel, C., 2008. Mechanical and electromagnetic properties of northern Gulf of Mexico sediments with and without THF hydrates, *Marine and Petroleum Geology*, 25(9), 884-895.

Lee, J. Y., Santamarina, J. C., Ruppel, C., 2010a. Parametric study of the physical properties of hydrate‐bearing sand, silt, and clay sediments: 1. Electromagnetic properties, *Journal of Geophysical Research: Solid Earth*, 115: B11104.

Lee, J. Y., Francisca F. M., Santamarina, J. C., Ruppel, C., 2010b. Parametric study of the physical properties of hydrate-bearing sand, silt, and clay sediments: 2. small-strain mechanical properties. Journal of Geophysical Research, 115: B11105.

Lee, J. Y., Yun, T. S., Santamarina, J. C., Ruppel, C., 2007. Observations related to tetrahydrofuran and methane hydrates for laboratory studies of hydrate-bearing sediments, *Geochemistry, Geophysics, Geosystems*, 8(6), 1-10.

Lei, L., Seol, Y., Choi, J. H., Kneafsey, T. J., 2019. Pore habit of methane hydrate and its evolution in sediment matrix-Laboratory visualization with phase-contrast micro-CT, *Marine and Petroleum Geology*, 104, 451-467.

Leroy, P., Revil, A., Kemna, A., Cosenza, P., Ghorbani, A., 2008. Complex conductivity of water-saturated packs of glass beads, *Journal of Colloid and Interface Science*, 321(1), 103-117.

Li, C., Liu, C., Hu, G., Sun, J., Hao, X., Liu, L., Meng, Q., 2019. Investigation on the multiparameter of hydrate‐bearing sands using nano-focus X-ray computed tomography, *Journal of Geophysical Research: Solid Earth*, 124(3), 2286-2296.

Liu, S., Han, T., Hu, G., Bu, Q., 2020. Dielectric behaviors of marine sediments for reliable estimation of gas hydrate saturation based on numerical simulation, *Journal of Natural Gas Science and Engineering*, 73,

103065.

Liu, Z., Ning, F., Hu, G., Liu, L., Liu, C., Peng, L., et al., 2008. Characterization of seismic wave velocity and attenuation and interpretation of tetrahydrofuran hydrate-bearing sand using resonant column testing, *Marine and Petroleum Geology*, 122, 104620.

Lv, J., Cheng, Z., Xue, K., Liu, Y., Mu, H., 2020. Pore-scale morphology and wettability characteristics of xenon hydrate in sand matrix-Laboratory visualization with micro-CT, *Marine and Petroleum Geology*, 120, 1-9.

Mahabadi, N., Dai, S., Seol, Y., Jang, J., 2019. Impact of hydrate saturation on water permeability in hydrate-bearing sediments, *Journal of Petroleum Science and Engineering*, 174, 696-703.

Mahabadi, N., Dai, S., Seol, Y., Sup Yun, T., Jang, J., 2016. The water retention curve and relative permeability for gas production from hydrate‐bearing sediments: Pore-network model simulation, *Geochemistry, Geophysics, Geosystems*, 17(8), 3099-3110.

Makogon, Y. F., 2010. Natural gas hydrates – A promising source of energy, J*ournal of Natural Gas Science and Engineering*, 2(1), 49-59.

Niu, Q., Zhang, C., 2017. Pore-scale modelling of complex conductivity of saturated granular materials, *Near Surface Geophysics*, 15(6), 593-602.

Niu, Q., Prasad, M., Revil, A., Saidian, M., 2016a. Textural control on the quadrature conductivity of porous media, *Geophysics*, 81(5), E297-E309.

Niu, Q., Revil, A., Saidian, M., 2016b. Salinity dependence of the complex surface conductivity of the Portland sandstone, *Geophysics*, 81(2), D125-D140.

Osterman, G., Keating, K., Binley, A., Slater, L., 2016. A laboratory study to estimate pore geometric parameters of sandstones using complex conductivity and nuclear magnetic resonance for permeability prediction, *Water Resources Research*, 52(6), 4321-4337.

Pan, H., Li, H., Chen, J., Zhang, Y., Cai. S., Huang Y., et al., 2020a. A unified contact cementation theory for gas hydrate morphology detection and saturation estimation from elastic-wave velocities, *Marine and*

Petroleum Geology, 113, 104146.

Pan, H., Li, H., Chen, J., Riedel, M., Holland, M., Zhang, Y., et al., 2020b. Quantification of gas hydrate saturation and morphology based on a generalized effective medium model, *Marine and Petroleum Geology*, 113, 104166.

Pan, L., Lei, L., Seol, Y., 2021. Pore-scale influence of methane hydrate on permeability of porous media, *Journal of Natural Gas Science and Engineering*, 87, 103758.

Revil, A., 2012. Spectral induced polarization of shaly sands: Influence of the electrical double layer, *Water Resources Research*, 48(2), 1-23.

Revil, A., 2013. Effective conductivity and permittivity of unsaturated porous materials in the frequency range 1 mHz-1GHz, *Water Resources Research*, 49(1), 306-327.

Revil, A., Coperey, A., Deng, Y., Cerepi, A. Seleznev, N., 2017a. Complex conductivity of tight sandstones, *Geophysics*, 83(2), 55-74.

Revil, A., Coperey, A., Shao, Z., Florsch, N., Fabricius, I. L., Deng, Y., et al., 2017b. Complex conductivity of soils, *Water Resources Research*, 53(8), 7121-7147.

Revil, A., Eppehimer, J. D., Skold, M., Karaoulis, M., Godinez, L., Prasad, M., 2013. Low-frequency complex conductivity of sandy and clayey materials, *Journal of Colloid and Interface Science*, 398, 193-209.

Revil, A., Koch, K., Holliger, K., 2012. Is it the grain size or the characteristic pore size that controls the induced polarization relaxation time of clean sands and sandstones?, *Water Resources Research*, 48(5), 1-7.

Revil, A., Linde, N., Cerepi, A., Jougnot, D., Matthäi, S., Finsterle, S., 2007. Electrokinetic coupling in unsaturated porous media, *Journal of Colloid and Interface Science*, 313(1), 315-327.

Revil, A., Skold, M., 2011. Salinity dependence of spectral induced polarization in sands and sandstones, *Geophysical Journal International*, 187(2), 813-824.

Schmutz, M., Blondel, A., Revil, A., 2012. Saturation dependence of the quadrature conductivity of oil-bearing sands, *Geophysical Research Letters*, 39(3), 1-6.

Schmutz, M., Revil, A., Vaudelet, P., Batzle, M., Viñao, P. F., Werkema, D. D., 2010. Influence of oil

saturation upon spectral induced polarization of oil-bearing sands, *Geophysical Journal International*, 183(1), 211-224.

Sell, K., Saenger, E. H., Falenty, A., Chaouachi, M., Haberthür, D., Enzmann, F., et al., 2016. On the path to the digital rock physics of gas hydrate-bearing sediments–processing of in situ synchrotron-tomography data, *Solid Earth*, 7(4), 1243-1258.

Sen, P. N., Goode, P. A., 1992. Influence of temperature on electrical conductivity on shaly sands, *Geophysics*, 57(1), 89-96.

Sloan, E. D., 2003. Fundamental principles and applications of natural gas hydrates. Nature, 426: 353-359.

Song, Y., Wang, S., Yang, M., Liu, W., Zhao, J., Wang, S., 2015. MRI measurements of CO_2-CH_4 hydrate formation and dissociation in porous media, *Fuel*, 140, 126-135.

Spangenberg, E., 2001. Modeling of the influence of gas hydrate content on the electrical properties of porous sediments, *Journal of Geophysical Research: Solid Earth*, 106(B4), 6535-6548.

Spangenberg, E., Kulenkampff, J., 2006. Influence of methane hydrate content on electrical sediment properties, *Geophysical Research Letters*, 33(24), 1-5.

Spangenberg, E., Kulenkampff, J., Naumann, R., Erzinger, J., 2005. Pore space hydrate formation in a glass bead sample from methane dissolved in water, *Geophysical Research Letters*, 32(24), 1-4.

Ta, X. H., Yun, T. S., Muhunthan, B., Kwon, T. H., 2015. Observations of pore-scale growth patterns of carbon dioxide hydrate using X-ray computed microtomography, *Geochemistry, Geophysics, Geosystems*, 16(3), 912-924.

Tarasov, A., Titov, K., 2013. On the use of the Cole-Cole equations in spectral induced polarization, *Geophysical Journal International*, 195(1), 352-356.

Waite, W. F., Santamarina, J. C., Cortes, D. D., Dugan, B., Espinoza, D. N., Germaine, J., et al., 2009. Physical properties of hydrate-bearing sediments, *Reviews of Geophysics*, 47(4), 1-38.

Waite, W. F., Winters, W. J., Mason, D. H., 2004. Methane hydrate formation in partially water-saturated Ottawa sand, *American Mineralogist*, 89(8-9), 1202-1207.

Wang, D., Li, Y., Liu, C., Zhan, L., Lu, H., Li, C., et al., 2020. Study of hydrate occupancy, morphology and microstructure evolution with hydrate dissociation in sediment matrices using X-ray micro-CT, *Marine and Petroleum Geology*, 113, 1-11.

Wang, Q., Han, D., Wang, Z., Ma, Q., Wang, D., 2019. Lattice Boltzmann modeling for hydrate formation in brine, *Chemical Engineering Journal*, 366, 133-140.

Waxman, M. H., Smits, L. J. M., 1968. Electrical conductivities in oil-bearing shaly sands, *Society of Petroleum Engineers Journal*, 8(02), 107-122.

Worthington, P. F., Collar, F. A., 1984. Relevance of induced polarization to quantitative formation evaluation, *Marine & Petroleum Geology*, 1(1), 14-26.

Xing, L., Zhu, T., Niu, J., Liu, C., Wang, B., 2020. Development and validation of an acoustic-electrical joint testing system for hydrate-bearing porous media, *Advances in Mechanical Engineering*, 12(3), 1-11.

Yang, L., Zhao, J., Liu, W., Li, Y., Yang, M., Song, Y., 2015. Microstructure observations of natural gas hydrate occurrence in porous media using microfocus X-ray computed tomography, *Energy & Fuels*, 29(8), 4835-4841.

Yu, P. Y., Sean, W. Y., Yeh, R. Y., Hsieh, L. H. C., Hsu, R. Q., Sato, T., 2017. Direct numerical simulation of methane hydrate dissociation in pore-scale flow by using CFD method, *International Journal of Heat and Mass Transfer*, 113, 176-183.

Yun, T. S., Francisca, F. M., Santamarina, J. C., Ruppel, C., 2005. Compressional and shear wave velocities in uncemented sediment containing gas hydrate, *Geophysical Research Letters*, 32(10), 1-5.

Zhao, J., Yang, L., Liu, Y., Song, Y., 2015. Microstructural characteristics of natural gas hydrates hosted in various sand sediments, *Physical Chemistry Chemical Physics*, 17(35), 22632-22641.